

10 **Supplementary Material**

11 **S1. Review of Airborne Arctic Methane measurements**

12 CH₄ concentration profiles over the Arctic Ocean were measured on five flights during the HIAPER Pole-to-Pole
13 Observations (HIPPO) campaign [E A Kort *et al.*, 2012; S C Wofsy, 2011] and produced evidence of sea surface CH₄
14 emissions from the northern Chukchi and Beaufort Seas in most profiles, up to 82°N. Enhanced concentrations near
15 the sea surface were common over fractured floating ice in sample profiles collected on 2 Nov. 2009, 21 Nov. 2009,
16 and 15 Apr. 2010. On 13 Jan. 2009 and 26 Mar. 2010, when the seasonally highest level of sea-ice coverage occurred,
17 CH₄ emissions were weak or non-existent. Some of the observational variability was correlated with carbon monoxide
18 (CO), indicating terrestrial origin.

19 The Carbon in Arctic Reservoirs Vulnerability Experiment (CARVE) program sought to quantify Alaskan CO₂ and
20 CH₄ fluxes between the atmosphere and surface terrestrial ecosystems. Intensive aircraft campaigns with ground-
21 based observations were conducted during summer from 2012-2015 [R Y-W Chang *et al.*, 2014]. No open ocean
22 measurements were made. Additional Alaskan airborne data were collected summer 2015 (Jun.-Sept.) by the
23 Atmospheric Radiation Measurements V on the North Slope of Alaska (ARM-ACME) project (38 flights, 140 science
24 flight hours), with vertical profile spirals from 150 m to 3 km over Prudhoe Bay, Oliktok Point, Barrow, Atkasuk,
25 Ivtok, and Toolik Lake. Continuous data on CO₂, CH₄, CO, and nitrous oxide, N₂O, were collected [S C Biraud,
26 2016].

27 West of Svalbard, an area of known widespread seabed CH₄ seepage aligned along a north-south fault parallel to the
28 coast [S Mau *et al.*, 2017; G K Westbrook *et al.*, 2008] was the focus of a field airborne campaign June–July 2014 [C
29 L Myhre *et al.*, 2016]. Flights were conducted using the Facility for Airborne Atmospheric Measurements (FAAM)
30 of the Natural Environment Research Council (NERC, UK). The campaign measured a suite of atmospheric trace
31 gases and was coordinated with oceanographic observations. Seabed CH₄ seepage led to significantly increased
32 seawater CH₄ concentrations. However, no significant atmospheric CH₄ enhancement was observed for the region
33 above the seeps for summer data collected 20 Jun.–1 Aug. 2014 [C L Myhre *et al.*, 2016] under mostly light winds.

34

35 **S2. Satellite Arctic AIRS and IASI Methane Measurement and Validation**

36 A number of current orbital TIR instruments observe CH₄ [D J Jacob *et al.*, 2016] including the Tropospheric Emission
37 Spectrometer (TES) [J Worden *et al.*, 2012], the Cross-Track Infrared Sounder (CrIS) [A Gambacorta, 2013], InfraRed
38 Atmospheric Sounder Interferometer (IASI) [C Clerbaux *et al.*, 2009], and the Atmospheric Infrared Sounder (AIRS)
39 [Hartmut H. Aumann *et al.*, 2003].

40 IASI CH₄ validation has been addressed in a number of studies for the lower and mid-upper Arctic troposphere. The
41 EuMetSat IASI instruments are cross-track-scanning Michelson interferometers onboard the MetOp-A and MetOp-B
42 platforms [C Clerbaux *et al.*, 2009]. IASI-1 (2007-) and IASI-2 (2013-) follow sun synchronous orbits. Three IASI
43 New Generation instruments [C Crevoisier *et al.*, 2014] are planned for launch in 2021, 2028, and 2035 [IASI-NG,
44 2017].

45 IASI instruments measure in 8461 channels at 0.5 cm⁻¹ spectral resolution from three spectrometers spanning 645 to
46 2760 cm⁻¹. These spectrometers have a 2×2 array of circular footprints with a nadir spatial resolution of 12 km that is
47 39×25 km at swath (2400 km) maximum [C Clerbaux *et al.*, 2009]. IASI-1 was launched into an 817 km-altitude polar
48 orbit on 19 Oct. 2006, while IASI-2 was launched on 17 Sept. 2012. MetOp-A and MetOp-B cross the equator at
49 approximately 09:30 and 21:30 local time, separated by approximately half an orbit, resulting in twice daily, near-
50 global coverage with 29-day revisit. The on-flight noise-equivalent delta temperature at 280K is estimated to be well
51 below 0.1K in the spectral range of interest to CH₄ [A Razavi *et al.*, 2009]. IASI has a wide swath with a scan angle
52 of ±48.3°. IASI CH₄ retrieval algorithms are described by X Xiong *et al.* [2013] and A Gambacorta [2013].

53 In the TIR, the AIRS (Atmospheric InfraRed Sounder) mission onboard the Earth Observation Satellite, Aqua satellite
54 [Hartmut H. Aumann *et al.*, 2003] and the EuMetSat IASI-1 mission, on the MetOp-A platform [C Crevoisier *et al.*,
55 2014] [C Clerbaux *et al.*, 2009] provide long-term arctic CH₄ observations with new IASI instruments planned for
56 launch in 2021, 2028, and 2035 [IASI-NG, 2017].

57 AIRS is a grating diffraction nadir cross-track scanning spectrometer on the Aqua satellite (2002-) that is part of the
58 Earth Observation System [H.H. Aumann *et al.*, 2003]. AIRS was launched into a 705-km-altitude polar orbit on the
59 EOS Aqua spacecraft on 4 May 2002. The satellite crosses the equator at approximately 01:30 and 13:30 local time,
60 producing near global coverage twice a day, with a scan angle of $\pm 48.3^\circ$. Effective field of view after cloud clearing,
61 is 45 km [J Susskind *et al.*, 2006] and the CH₄ spectral resolution is 1.5 cm⁻¹ from the 7.8 μm TIR channel [Hartmut
62 H. Aumann *et al.*, 2003]. Version 6 of AIRS Levels 2 and 3 data are publicly available [AIRS, 2016]; see X Xiong *et al.*
63 *al.* [2010] for a description, evaluation, and validation of global CH₄ AIRS retrievals. Lower-troposphere (0-4 km
64 altitude averaged) AIRS profiles are analyzed herein because the AIRS time series is longer than IASI.

65 AIRS CH₄ validation has been addressed in X Xiong *et al.* [2010], who compared aircraft data taken over Poker Flat,
66 Alaska, and Surgut, Siberia with AIRS CH₄ retrieved profiles. Agreement was within 1.2% with mean measured CH₄
67 concentration between 300–500 hPa; correlation coefficients were ~ 0.6 – 0.7 .

68 IASI validation [X Xiong *et al.*, 2013] over a large area was achieved during a quasi pole-to-pole flight of the
69 National Science Foundation's Gulfstream V aircraft [S C Wofsy, 2011]. A bias of nearly -1.74% was found for 374–
70 477 hPa and -0.69% for 596–753 hPa. L Yurganov *et al.* [2016] compared 5-year long IASI data for 0-4 km layer over
71 a sea area adjacent to the Zeppelin Observatory, Svalbard, Norway, at 474 m altitude, operated by the Norwegian
72 Institute for Air Research (NILU). Monthly mean values and monthly trends were in good agreement, but daily
73 excursions did not correlate. L Yurganov *et al.* [2016] explained the latter by the observatory's location being near the
74 top of the planetary boundary layer.

75

76 **S3. Currents**

77 **S3.1. Barents and Kara Sea Currents**

78 The Barents Sea is bounded to the south by northern Europe and to the north by two archipelagos, Svalbard and Franz
79 Josef Land (FJL). To the east lies the large north-south oriented, Novaya Zemlya archipelago, beyond which is the
80 Kara Sea; to the west lies the Norwegian Sea. In winter the Barents Sea is partially ice-covered, while it is almost ice-
81 free in the summer

82 The North Atlantic is a significant source of Arctic Basin water, whose density increases by cooling. Some of this
83 water flows into the Barents Sea, ~ 2 Sv (1 Sv = 10^6 m³ s⁻¹), varying seasonally [H Loeng *et al.*, 1997] with most
84 returning to the North Atlantic as part of the global thermohaline circulation [K Aagaard and E C Carmack, 1989; E
85 Carmack and F McLaughlin, 2011; M Yamamoto-Kawai *et al.*, 2008]. T A McClimans and J H Nilsen [1993] used a
86 laboratory physical model simulation to duplicate most of the observed regional Barents Sea oceanographic features
87 forced by the densities and volume fluxes of water from the Atlantic (the Norwegian Atlantic Current - NAC and the
88 Norwegian Coastal Current - NCC) and Arctic Basin (Persey Current - PC) and Barents Sea hydrography. Key features
89 produced were the general structure of fronts and major currents, etc., which were obtained without regional
90 atmospheric forcing. This highlights the dominant importance of oceanography rather than meteorology to these
91 features.

92 North Atlantic water flows through the Norwegian Sea, forming the NAC, one track of which becomes the West
93 Spitsbergen Current (WSC), with the remainder flowing into the Barents Sea through the Barents Sea Opening as the
94 North Cape Current [J Piechura and W Walczowski, 2009]. The North Cape Current bifurcates into several forks
95 mostly flowing to the east along the southern slope of the Barents Sea becoming the Murman Current (MC) near
96 Murman.

97 The NAC is the major contributor of oceanic heat to the Barents Sea [V S Lien *et al.*, 2017]. Regional winds modulate
98 the volume flow of Atlantic water into the Barents Sea—stronger in winter and weaker in summer [J E Stiansen *et al.*,
99 2009; Fig. 2.3.4]. Ice processes further complicate heat re-distribution for surface Arctic Ocean waters – ice insulates
100 the water (better preserving the water’s heat) from atmospheric radiative cooling. For example, the NAC’s western
101 fork (the WSC) submerges north of Spitsbergen (location varying seasonally) under an isolating layer of colder and
102 fresher water furthering heat transport into the Arctic [V S Lien *et al.*, 2013; V S Lien *et al.*, 2017].

103 A south fork of the NAC is entrained into the NCC, which is 90% Atlantic water and 10% river discharge [Ø Skagseth
104 *et al.*, 2008]. The NCC is a major contributor of oceanic heat to much of the southern and eastern Barents Sea and into
105 the Kara Sea [V S Lien *et al.*, 2013]. The NCC cools significantly through interaction with the atmosphere. Upon
106 entering Russian waters, the NCC is renamed the Murman Coastal Current (MCC). Long-term (1905-) temperature
107 data for the upper 200 m are available from a section off the Kola Peninsula (**Fig. 4a, Kola Section, black dashed**
108 **line**), which the MCC crosses [V D Boitsov *et al.*, 2012]. These data reveal long-term trends with a cooler period from
109 1875-1930 and continuous warming of ~0.8°C since a minimum in 1970-1980 [Ø Skagseth *et al.*, 2008]. The Kola
110 Section data (which is full water column) show good gross agreement with long-term (since 1850) Barents Sea ice-
111 extent [J E Walsh *et al.*, 2016] – the warm period from 1930-1965 corresponds to a significant reduction of spring
112 sea-ice (from ~0.2 to ~0.12). The Kola Section data shows steady warming since 1970 that corresponds to a consistent
113 general sea-ice extent decrease since 1980 in spring and since 1970 in fall. This highlights that important long
114 timescale forcing by the MC and MCC affects sea ice extent, meteorology, and oceanography in the southern and
115 eastern Barents Sea.

116 Although beyond this study’s scope, changes in the NAC/MC flow through the Kola Section relate to larger
117 oceanographic trends. Ø Skagseth *et al.* [2008] found good agreement in the Kola Section temperature trend with the
118 Atlantic Multi-decadal Oscillation (AMO) index. SST lags atmospheric temperatures by 2-3 months, peaking for the
119 Kola area (offshore Murman, Russia) between 0 and 200 m in September-October, whereas air temperature peaks in
120 July [J E Stiansen *et al.*, 2009, Figs. 2.3.3, 2.3.8].

121 The MCC continues eastward along the northern edge of the White Sea, becoming the Novaya Zemlya Current (NZC)
122 until diverted northwards by Novaya Zemlya. It continues into the Arctic Basin through the Saint Anna Trough (SAT)
123 between Franz Josef Land and Novaya Zemlya [H Loeng, 1991], which is the dominant outflow of the Barents Sea
124 [W Maslowski *et al.*, 2004]. A fork of the MCC flows eastward into the Kara Sea through the narrow and shallow (20-
125 50 m) Kara Strait (**Supp. Fig. S1** shows detailed Kara Sea currents).

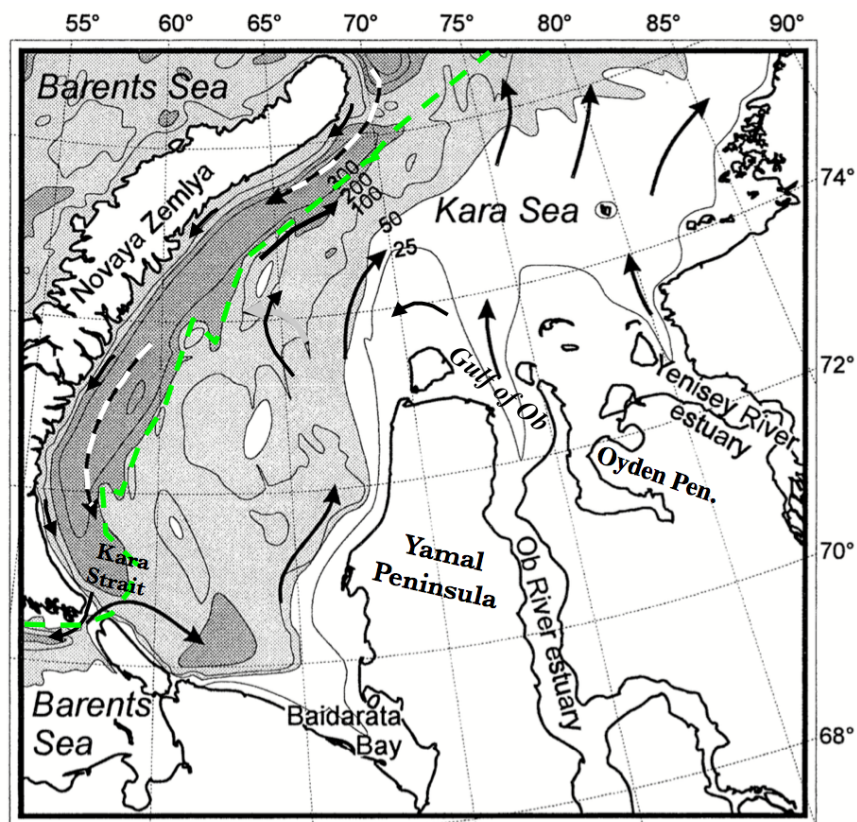
126 A fork of the North Cape Current flows north through the Bear Island Channel towards the Hopen Deep (Loeng *et al.*,
127 1997), underneath the cold, south-flowing Bear Island Current (BIC). J A Whitehead and J Salzig [2001] suggested
128 (and demonstrated in the laboratory) that remote forcing of the NAC through the Barents Sea lifts the current by
129 several hundred meters to the sill of the Bear Island Channel, forcing significant anticyclonic vorticity. This drives the
130 retrograde Bear Island Channel Current (BICC, our connotation) northeast along the slope of Svalbard Bank and the
131 prograde Murman Current (MC) along the slope of Tromsøflaket, eastward and north to the east of the Central and
132 Great Banks [S Li and T A McClimans, 1998; H Loeng, 1991]. S Li and T A McClimans [1998] referred to the BICC
133 as the “Warm Core Jet” to emphasize its physical significance at the Polar Front. These merge east of the Central and
134 Great Banks. The resulting flow cools from contact with the atmosphere into a denser, modified Atlantic Water flow
135 that exits through the Saint Anna Trough to the east of Franz Joseph Land [T Gammelsrød *et al.*, 2009]. Cooling at
136 these banks also produces a dense westward underflow, depicted by the dashed line in **Fig. 4a**.

137 The Percey Current transports cold, low saline, Arctic surface water into the Barents Sea to the east of Spitsbergen,
138 becoming the Bear Island Current (BIC) to the west of the Grand Bank (**Supp. Fig. S2**). The Percey Current meets
139 warmer, higher salinity waters of Atlantic origin in the Barents Sea, giving rise to the Barents Sea Polar Front [L Oziel
140 *et al.*, 2016], whose location is controlled by seabed bathymetry, i.e., it is semi-stationary [G Gawarkiewicz and A J
141 Plueddemann, 1995]. This front is part of a unique frontal system due to its combination with the seasonally ice-
142 covered zones in the northern, central, and eastern Barents Sea [T Vinje and Å S Kvambekk, 1991]. Part of the Percey
143 Current merges with the East Spitsbergen Current (ESC) to the west of the Svalbard Bank and then flows north along

144 the west Spitsbergen coast, inshore of the WSC, as the Spitsbergen Coastal Current (SCC). This flow loops the Barents
145 Sea Polar Front around Spitsbergen [H Svendsen *et al.*, 2002].

146

147 S3.2. Detailed Kara Sea Currents and Bathymetry



148

149 **Figure S1.** Bathymetry and currents for the Kara Sea. Adapted from *L Polyak et al.* [2002] and *T A McClimans et al.*
150 [2000]. Dashed line indicates subsurface flows. Green line shows approximate edge of submerged permafrost from *T*
151 *E Osterkamp* [2010].

152 Kara Sea hydrography is controlled by the freshwater outflow of the Ob and Yenisei Rivers (**Fig. 2b; Supp. Fig. S1**
153 **for finer details**), which contribute 350 and 650 km³ yr⁻¹, respectively [C A Stedmon *et al.*, 2011], approximately
154 double that of the Mississippi River, primarily (>75%) between May and September. As a result, the eastern Kara Sea
155 is brackish. Riverine sediment leads to the northeast Kara Sea being mostly shallow (< 50 m). The western Kara Sea
156 is deep (mostly >100 m), descending to below 500 m in the Novaya Zemlya Trough [L Polyak *et al.*, 2002].

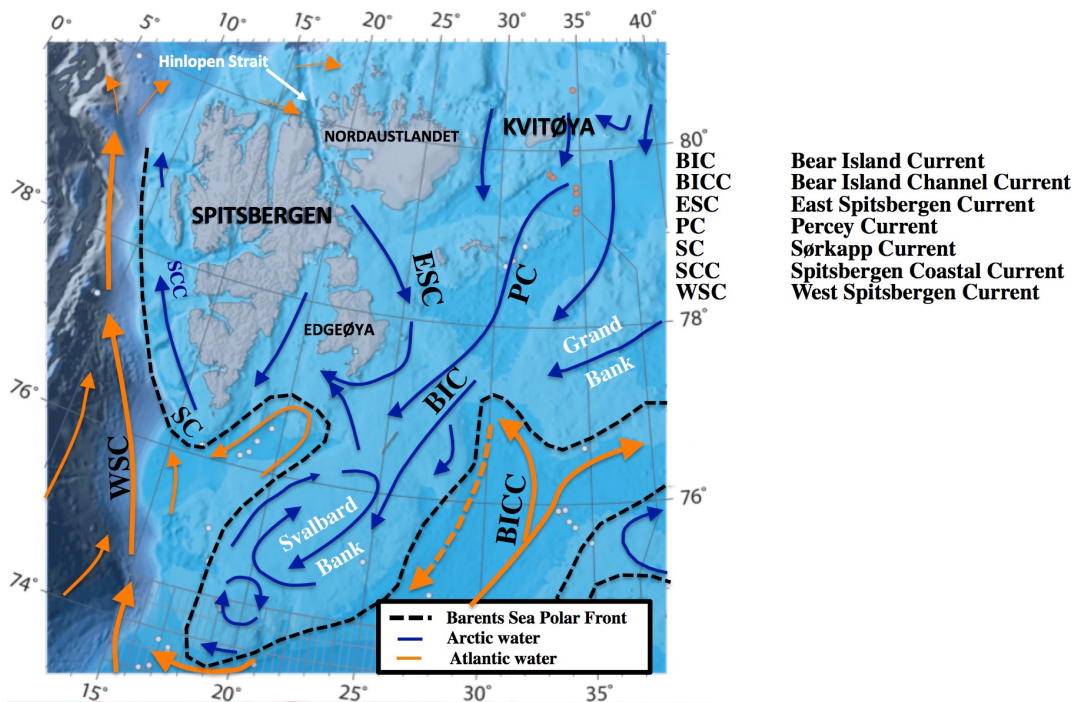
157 Cold Arctic waters, and ice and melt water from Novaya Zemlya flow southward along the eastern shore of the Novaya
158 Zemlya Archipelago in the narrow, weak Novaya Zemlya Coastal Current (NZCC). Inflow of modified Atlantic water
159 from the Barents Sea (dashed line in **Fig. S1**) accounts for a warm core in the deep Novaya Zemlya Trough [see *T A*
160 *McClimans et al.*, 2000, Section 11]. Part of the NZCC exits through the same Kara Strait that Barents Sea coastal
161 water enters. This, in combination with the rising shallow seabed, causes the Kara Strait to be a site of strong mixing.

162 Deeper water in the trough is supplied by inflow of modified Atlantic water from the northern Barents Sea. On the
163 surface, inflows to the north Kara Sea come from the MCC, local runoff, and ice in the Novaya Zemlya Coastal
164 Current (NZCC), with some flow returning to the Barents Sea through the Kara Strait. Warmer water enters the south
165 Kara Sea from the Barents Sea as the MCC flows through the Kara Strait, joining a northward flowing slope current.

166 Much of this water mixes with the southern flowing NZCC and returns to the Barents Sea through the Kara Strait [T
 167 A McClimans *et al.*, 1999; T A McClimans *et al.*, 2000].

168 The Ob and Yenisei Rivers transport significant sediment, underlying the shallowness of the Kara Sea, with extensive
 169 proven and proposed petroleum hydrocarbon reservoirs underlying the east and southeast Kara Sea [P Rekacewicz,
 170 2005]. Given the Kara Sea's shallowness, CH₄ seep seabed bubbles can mostly transfer their gas directly to the
 171 atmosphere [I Leifer and R Patro, 2002; I Leifer *et al.*, 2017] and indirectly from wind mixing [R Wanninkhof and W
 172 R McGillis, 1999], and also from storm sparging [V D Boitsov *et al.*, 2012; N Shakhova *et al.*, 2013], which in the
 173 Arctic can extend to 100-200 m depth, i.e., most of the Kara Sea.

174 **S3.3. Detailed West Barents Sea Currents and Bathymetry**



175 **Figure S2.** Bathymetry and currents around Svalbard. Bathymetry from *Norwegian Petroleum Directorate* [2016].
 176 Currents from *H Loeng* [1991]. Dashed black line shows location of the Barents Sea Polar Front, Dashed currents are
 177 submerged; blue - cold, orange - warm.
 178

179 Currents and flows around Svalbard Archipelago are complex (**Fig. S2**), dominated by the West Spitsbergen Current
 180 (WSC), which is the northerly fork of the Norwegian Atlantic Current (NAC), and flows northwards off the west coast
 181 of Spitsbergen. The cold, Percey Current (PC) flows southwest off the eastern shores of the Svalbard Archipelago.
 182 The cold East Spitsbergen Current (ESC) flows through the Hinlopen Strait and then joins the PC to flow around the
 183 south cape of Spitsbergen as the Sørkapp Current (SC), following the coast northwards as the Spitsbergen Coastal
 184 Current (SCC) [H Svendsen *et al.*, 2002]. The cold SCC flows inshore of the WSC, and flows up Svalbard's western
 185 coast, inshore and shallower than the warm, Atlantic WSC. The interface between these two currents off west
 186 Spitsbergen forms a part of the Barents Sea Polar Front. Thus, coastal waters offshore West Spitsbergen are of Barents
 187 Sea / Atlantic water origin, whereas further offshore lies Barents Sea water (origin Atlantic Ocean).

188 The location of the Barents Sea Polar Front [L Oziel *et al.*, 2016] is semi-permanent and controlled by seabed
 189 topography (**Fig. S2**), particularly the Svalbard Bank, the Great Bank, and the trough south of Spitsbergen.

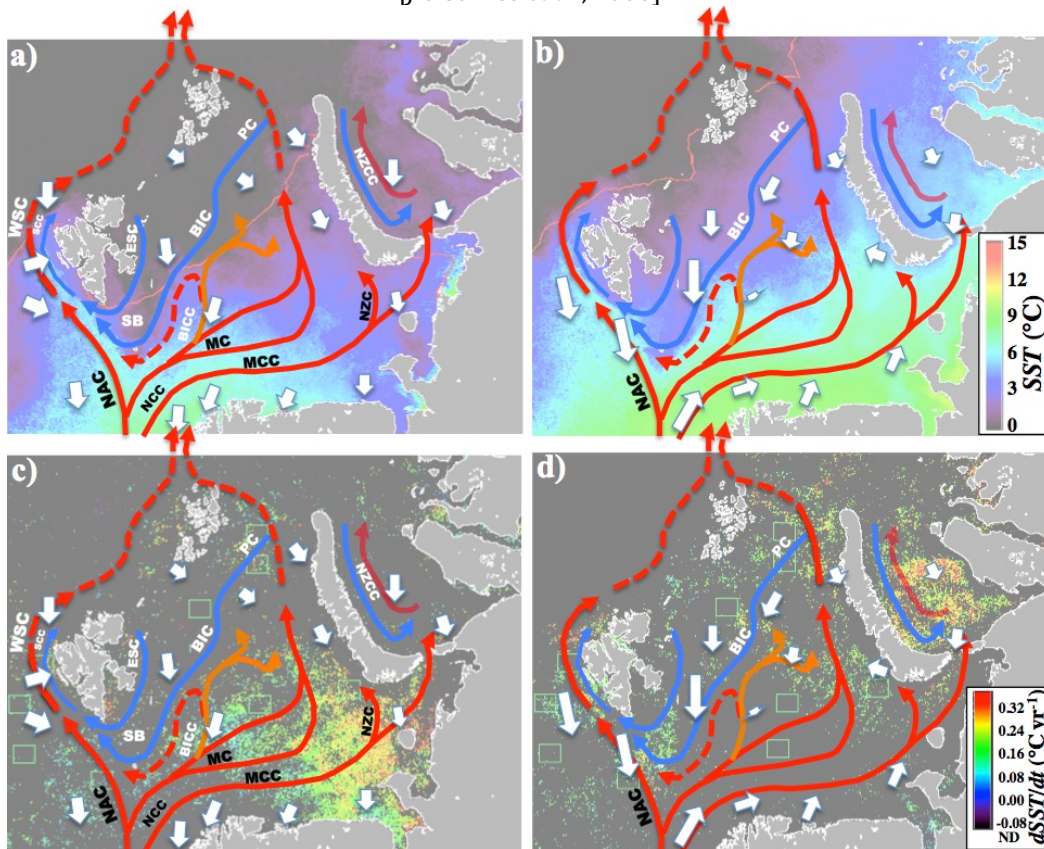
190 The energy budget of the Barents Sea is driven by Atlantic heat input by the two forks of the NAC (**Fig. S3**) [V S Lien
 191 *et al.*, 2013], strongly impacting the Barents Sea SST climatology (**Fig. S3**). Along one fork, warmer water flows

192 eastward along the northern Norwegian, Murman, and then western Novaya Zemlya coasts towards the north. The
 193 other NAC fork flows northeast along the Svalbard Bank (SB). These flows closely correspond to “tendrils” of warmer
 194 water extending north to the east of the Central Bank and to the west of Novaya Zemlya and around Bear Island (**Fig.**
 195 **S3a**) and in September in the east Barents Sea (**Fig. S3b**). In June, winds oppose this climatology, i.e., *SST* is most
 196 strongly influenced by ocean current transport. In fall, currents and winds are aligned along the Norwegian and
 197 Murman and western Novaya Zemlya coasts, reinforcing the transport of heat as indicated in *SST*. Note, though much
 198 of the heat that these winds transport originates from the NAC, which maintains Norway at temperatures well above
 199 latitudinal averaged. Still, winds cannot explain the spatial distribution of warm *SST*, which extends into the calm
 200 around the Central Bank.

201 Water becomes cooler as it penetrates eastward, and as it reaches the (seasonally varying) ice edge (**Fig. S3**). Across
 202 much of the Barents Sea there is a strong latitudinal *SST* gradient extending south from the ice edge, independent of
 203 the location of the eastern NAC branches. In the coastal waters off western Novaya Zemlya, where the warm NZC
 204 flows, water extends further north than elsewhere into areas where winds are from the north (**Fig. 4a**). Moreover,
 205 regions with statistically significant warming *SST* trends ($dSST/dt$) were in areas of northerly winds both in June and
 206 September.

207

[J C Comiso et al., 2008]

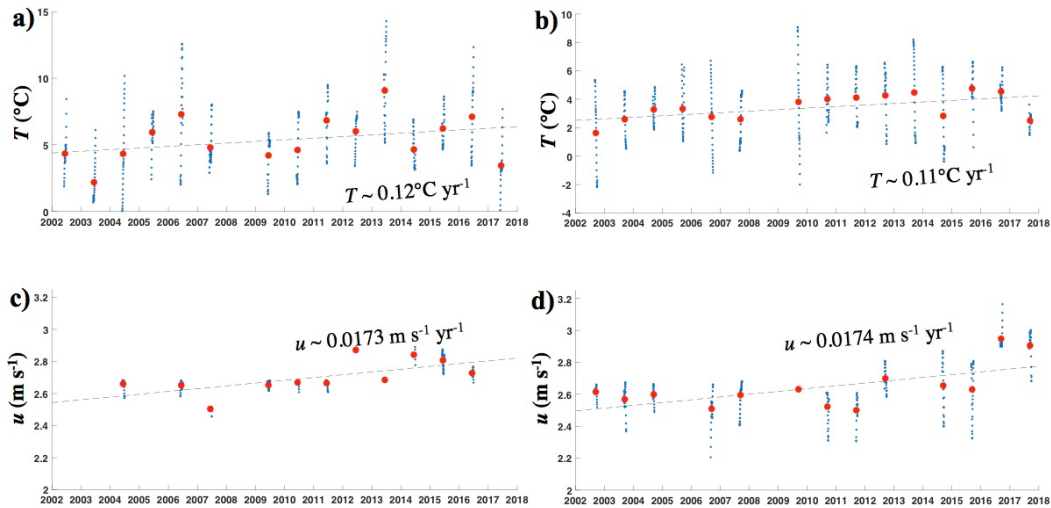


208
 209 **Figure S3.** Warm and cold currents (from **Fig. 4a**) superimposed on **a**) June and **b**) September for climatology *SST*,
 210 and **c**) June and **d**) September for $dSST/dt$ trends (ND-no trend detected). The red line shows ice location. Red and
 211 blue arrows show warm and cold currents, respectively. Dashed line indicates subsurface flow. Winds (white arrows)
 212 are adapted from *E W Kolstad* [2008].

213 **S4. Winds in the Barents and Kara Sea**

214 Accessible meteorological data for the Barents Sea, outside of west Svalbard, whose meteorology and oceanography
 215 are affected by the Greenland Sea, are difficult to find, e.g., *V D Boitsov et al.* [2012] for Bear Island, except for sites

216 on the northern Norwegian and Murman coasts. In this regard, the Murmansk airport weather data are the most
 217 eastward available long-term data representing southern Barents Sea, coastal meteorology and oceanography. Daily
 218 average meteorology data for 2002-2018 were downloaded (<https://www.wunderground.com/weather/ru/murmansk>)
 219 and segregated by month, and found a warming of $0.12^{\circ}\text{C yr}^{-1}$ in June and $0.11^{\circ}\text{C yr}^{-1}$ in September. Over this period,
 220 winds strengthened slightly ($0.0173\text{ m s}^{-1}\text{ yr}^{-1}$) with most of the increase in September occurring in 2017 and 2018
 221 (**Fig. S4**). These warming rates are significantly faster than those at Bear Island, which reflects both the greater
 222 moderation of the marine rather than coastal atmosphere and the influence of the cold Bear Island Current. Winter
 223 temperatures increased even faster.



224
 225 **Figure S4.** Wind and temperatures for Murmansk airport, Murman, Russia (68.7845°N , 32.7579°E) for **a)** June and
 226 **b)** September. Daily-averaged (blue) and monthly-averaged (red) data, and linear polynomial fits (red dashed line) are
 227 shown. Data from weatherunderground.com.

228 **S5. Focus Areas**

229 **Table S1.** Focused study area coordinates

| Area | Upper Left | Upper Right | Lower Left | Lower Right |
|------|------------------------------------|------------------------------------|--------------------------------------|------------------------------------|
| 1 | 79° 16'6.91" N 60° 48'53.42" E | 78° 32'12.26" N 62° 49'54.69" E | 78° 55' 5.27" N 57° 43' 42.58" E | 78° 12'27.81" N 59° 52'32.46" E |
| 2 | 78° 38'25.09" N 55° 34'48.90" E | 77° 56'45.71" N 57° 48'15.36" E | 78° 14' 20.21" N 52° 49' 55.73" E | 77° 34'0.24" N 55° 8'13.34" E |
| 3 | 79° 10'4.24" N 41° 13'50.40" E | 78° 36'13.19" N 44° 21'38.03" E | 78° 38' 35.38" N 38° 57' 26.67" E | 78° 6'12.61" N 42° 3'28.98" E |
| 4 | 79°38'46.04" N 5° 40'51.21" E | 79° 31'53.40" N 10° 11'25.49" E | 78° 57' 49.65" N 5° 19' 46.85" E | 78° 51'21.95" N 9° 34'7.45" E |
| 5 | 78° 8'40.32" N 0° 36'30.89" E | 78° 6'24.41" N 4° 35'53.20" E | 77° 27' 29.19" N 0° 34' 31.46" E | 77° 25'20.57" N 4° 20'54.29" E |
| 6 | 76° 11'22.21" N 1° 16'10.96" E | 76° 8'46.20" N 4° 41'44.27" E | 75° 30' 6.27" N 1° 12'35.25" E | 75° 27'37.48" N 4° 28'29.63" E |
| 7 | 74° 48'24.40" N 12° 40'7.63" E | 74° 36'9.07" N 15° 40'42.21" E | 74° 8' 1.53" N 12° 7'35.64" E | 73° 56'16.20" N 15° 1'6.10" E |
| 8 | 73° 34'52.37" N 33° 48'43.77" E | 73° 6'7.85" N 36° 8'55.31" E | 73° 0'12.51" N 32° 31'37.62" E | 72° 32'23.29" N 34° 49'20.56" E |
| 9 | 72° 46'29.04" N 48° 59'20.20" E | 72° 8'6.72" N 50° 44'6.03" E | 72° 18'49.49" N 47° 18'49.40" E | 71° 41'23.16" N 49° 4'27.27" E |
| 10 | 74° 48' 6.77" N 38° 38'57.13" E | 74° 16'3.18" N 41° 0'24.96" E | 74° 15'28.49" N 37° 5'34.21" E | 73° 44'27.53" N 39° 25'24.39" E |

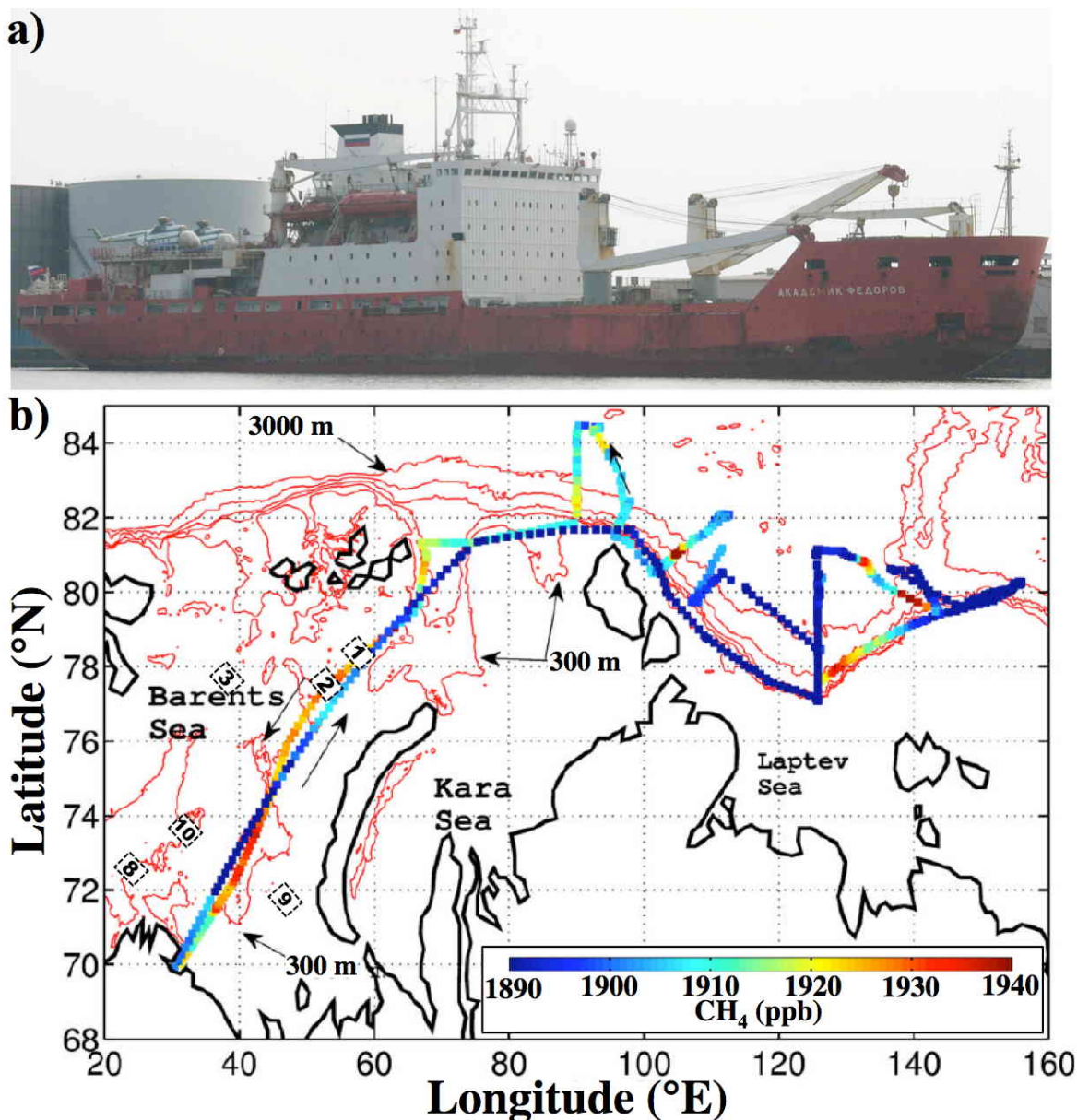
230

231

232 **S6. Barents Sea *in situ* data**

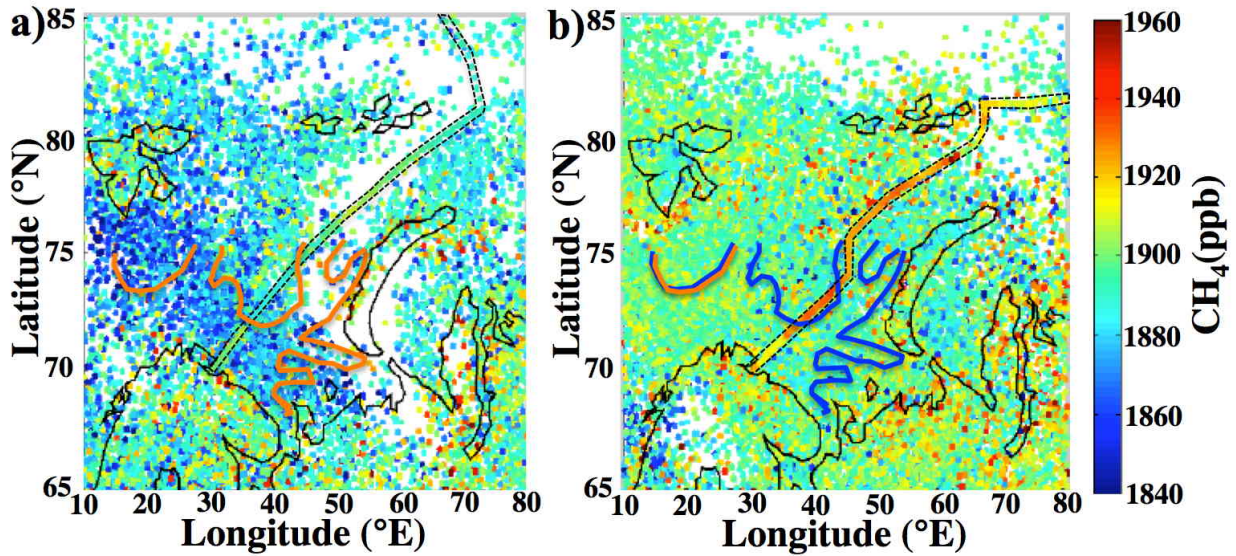
233 CO₂ and CH₄ *in situ* data were collected by a Cavity Enhanced Absorption Spectrometer (CEAS), Greenhouse Gas
234 Analyzer (Los Gatos, Research, Mountainview, CA) onboard the *R/V Akademik Fyodorov* during the Nansen and
235 Amundsen Basins Observational System (NABOS) expedition in fall 2013. The *R/V Akademik Fyodorov* is 141-m
236 long with a 25-m beam and 8-m draught. The *R/V Akademik Fyodorov* departed Kirkenes, Norway on 21 Aug. 2013,
237 returning to Kirkenes on 23 Sept. 2013. Analyzer performance information also was recorded for data quality review.
238 Instrument precision was ~1 ppb with a 10 s response time and a 117 s mean layback time. Samples were collected
239 from above the main superstructure, approximately 25 m above the sea surface (**Fig. S4a**), Calibration was daily and
240 used a cylinder standard provided by the Norwegian Air Research Institute (NILU).

241 The main potential source of ship pollution could be the diesel engine exhaust; however, it appears that the *Akademik*
242 *Fyodorov*'s engine is not a source of CH₄, with atmospheric CH₄ partially oxidized by the engine leading to exhaust
243 gas having depressed CH₄ compared to ambient air. Data analyzed herein were during steaming transit across the
244 Barents Sea at 26 km hr⁻¹, for which other potential vessel sources, such as the sewage storage venting are not relevant.



245
 246 **Figure S5.** a) Photo of the *R/V Akademik Fyodorov*. b) Hourly averaged methane (CH_4) from NABOS expedition.
 247 Red shows 300 m depth of the hydrate stability field. Location of focus areas (**Table S1**) shown. Data key on figure.

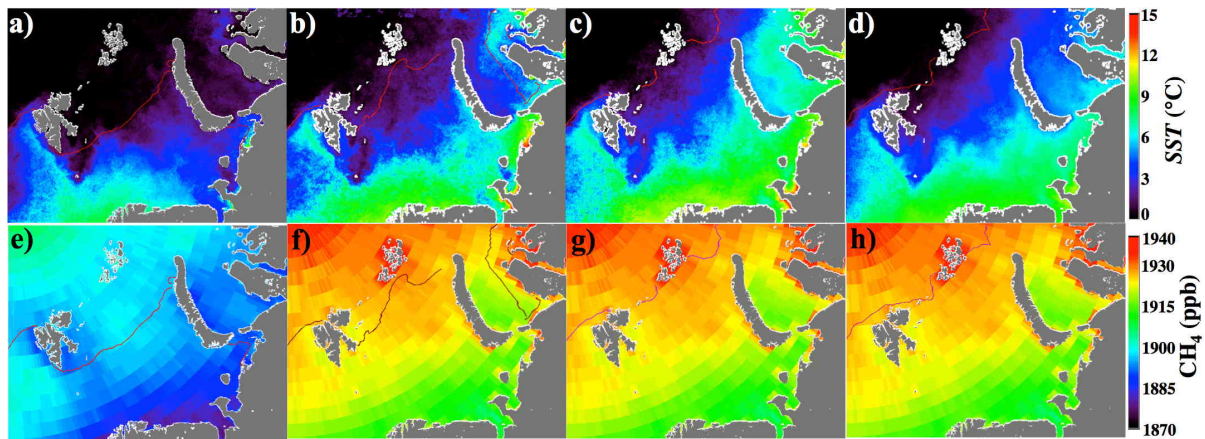
248 The month-long data set showed a significant difference between the northwards and southwards transits of the
 249 Barents Sea, which were separated by approximately one month and passed directly through Focus areas 1 and 2, as
 250 well as between focus areas 9 and 10 in the southeast Barents Sea, approximately along the path of the Murman
 251 Current. Most of the CH_4 values in the Laptev Sea were low, although there were several locations of enhanced CH_4 .
 252 NABOS values were compared with satellite-retrieved column CH_4 from IASI for 21-24 Aug. 2013 for the
 253 northeastwards transit and for 17-22 Sept. 2013 for the southwestwards transit. Agreement between IASI lower
 254 tropospheric CH_4 and *in situ* CH_4 for the northwards transit was good, within ~ 10 ppb, whereas agreement was much
 255 poorer for the southwards transit.



256
 257 **Figure S6.** a) IASI retrieved 0-4 km methane (CH_4) for 21-24 Aug. 2013 and hourly CH_4 from the NABOS cruise
 258 (outlined in dashed line black). Also shown is the Murman Coastal Current's edges in orange and blue from *A P*
 259 *Alexeev et al.* [2018] and b) for 17-22 Sept. 2013. Data key on figure.

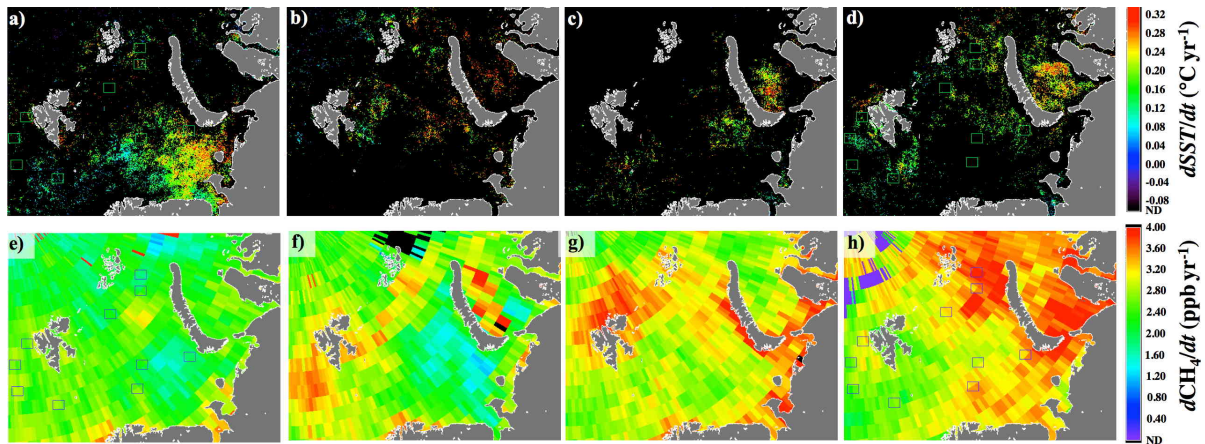
260

261 **S7. Summer month sea surface temperature and methane trends**



262
 263 **Figure S7.** Mean values for 2003 to 2015 of sea surface temperature (*SST*) for a) June, b) July, c) August, and d)
 264 September. Mean methane (CH_4) concentration for e) June, f) July, g) August, and h) September. Median ice edge for
 265 same period is shown. Years with reduced ice extent contribute to values of *SST* north of the ice edge. Data keys on
 266 figure.

267



268
 269 **Figure S8.** Linear trends for 2003 to 2015 of sea surface temperature ($dSST/dt$) for **a)** June, **b)** July, **c)** August, and **d)**
 270 September. Methane concentration trend (dCH_4/dt) for **e)** June, **f)** July, **g)** August, and **h)** September. ND – not
 271 detectable, i.e., failed statistical test. Blue, black dashed lines shows 100 and 50 m contour, respectively. Data key on
 272 figure.

273

274 **S8. Implications for Svalbard area methane emissions**

275 There are few atmospheric and ocean CH_4 data for the Barents Sea and surrounding areas, the most prominent being
 276 associated with CH_4 seepage off Spitsbergen, located immediately south of focus area A4. Studies to date have been
 277 in early summer; *S Mau et al.* [2017]; *C L Myhre et al.* [2016] sampled the atmosphere and water column while
 278 Westbrook et al. (2009) reported sonar observations of seep bubbles for August-September, and slightly elevated
 279 aqueous CH_4 in surface waters immediately above the bubble plumes. All concluded that transport to the atmosphere
 280 was not significant, attributed to trapping dissolved CH_4 below the pycnocline. It is important to note that with
 281 respect to the overall Barents Sea area CH_4 anomaly, the Svalbard area is far less important than waters around
 282 Franz Josef Land, off the west coast of Novaya Zemlya, and the north-central Barents Sea (**Fig. 9**).

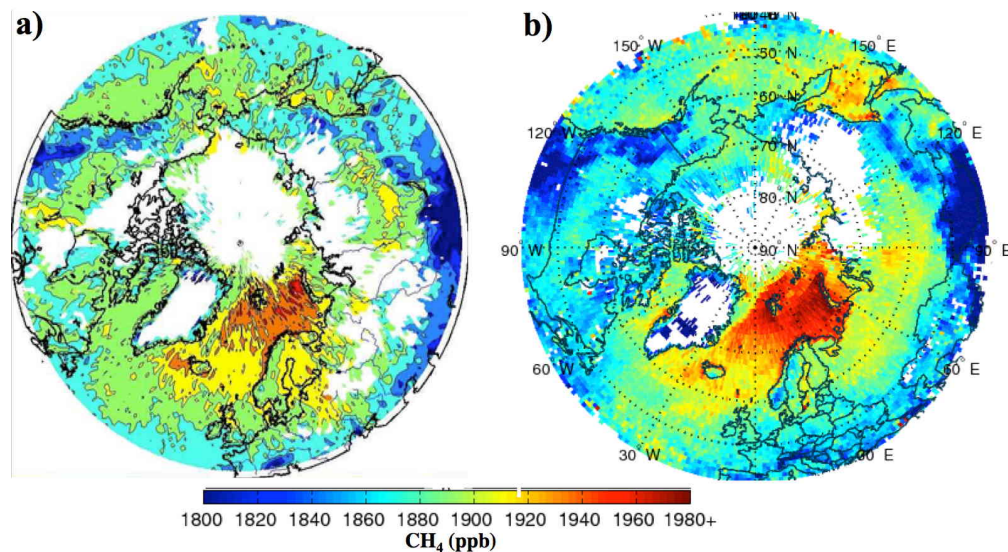
283 Both SST and CH_4 in June (**Fig. 9**) and July (**Supp. Fig. S7**) show that much of the active seepage in west
 284 Spitsbergen show that much of the area of active seepage was inshore of the Barents Sea Polar Front, and thus under
 285 the cooling Arctic waters of the Spitsbergen Coastal Current (SCC), supported by reported salinity data (Mau et al.,
 286 2017). Although SST remains low off Spitsbergen in September, and extends further offshore, CH_4 concentrations
 287 no longer are depressed compared to Atlantic water further offshore, i.e., greater transport to the atmosphere. Such
 288 transport would not be expected downcurrent (north) of the bubble plumes observed by the early fall cruise reported
 289 in *G K Westbrook et al.* [2009].

290 Although the studies indicate these seeps do not contribute to summer atmospheric CH_4 , they did not consider
 291 methane shoaling, which would allow seabed CH_4 to reach the atmosphere far downstream. Interestingly, Mau et al.
 292 (2017; Fig. 3) show data that could be interpreted as methane shoaling with elevated aqueous CH_4 forced shallower
 293 by the north-flowing SCC, crossing subterranean ridges. Focus area A4 shows the strongest increase in CH_4 from
 294 2005-and an increasing SST over this time period, consistent with shoaling. Stronger enhancement of CH_4 growth is
 295 observed north of Spitsbergen in June (**Fig. 10c**), which is the most likely location for shoaling based on detailed
 296 Svalbard bathymetry and currents (**Supp. Fig. S2**). Specifically, this is where some of the warm West Spitsbergen
 297 Current mixes with the cold, Spitsbergen Coastal Current (SCC) that would be CH_4 enriched from seabed seepage,
 298 and then flows over relatively shallow seabed towards the Hinlopen Strait. Thus, there is evidence of increasing
 299 downstream CH_4 transport to the atmosphere downcurrent of seepage off West Spitsbergen after methane shoaling,
 300 albeit not significant to overall Barents Sea emissions.

301 There is evidence of acceleration in the CH₄ growth nearshore off West Spitsbergen in June, but not in September
302 (**Fig. 10d**) when CH₄ growth enhancement lies in the further offshore waters that are impacted by the warm WSC.
303 Trends in *SST* also suggest a weakening of the Percey Current in June and more so in September. Given that from
304 June to September the SCC extends further offshore, this suggests WSC control. Similarly, the WSC eastwards leg
305 that crosses Nordaustlandet is driving a rapid increase in *SST* in September and likely relates to the increased CH₄
306 trend.

307

308 **S9. Arctic Methane Movie**



309

310 **Figure S9.** IASI Arctic methane (CH₄) for the lower 4 km for a) March 2012 and b) March 2018.

311 A movie of Arctic CH₄ from 2012 every 5 days shows a range of variations on a range of different spatial and temporal
312 scales (**Fig. S9**). Strong enhancements are observed that persist in regions for a few days—most likely related to
313 synoptic system flushing in fall to spring. The seasonal variation is easily observed, with highest values often in
314 November and December. In late winter and early spring, large CH₄ anomalies are observed in some years at the ice
315 edge.

316 **Supplemental References**

- 317 Aagaard, K., and E. C. Carmack (1989), The role of sea ice and other fresh water in the Arctic
318 circulation, *Journal of Geophysical Research: Oceans*, 94(C10), 14485-14498.
- 319 AIRS (2016), Version 6 AIRS Level 2 and 3 CH4 data, edited.
- 320 Alexeev, A. P., A. V. Semenov, V. A. Borovkov, V. V. Tereshchenko, and V. N. Shleinik (2018),
321 Historical review of oceanographic observations in the Kola section, edited, Polar Research
322 Institute of Marine Fisheries and Oceanography (PINRO), Murmansk, Russia.
- 323 Aumann, H. H., et al. (2003), AIRS/AMSU/HSB on the Aqua mission: design, science objectives,
324 data products, and processing systems, *IEEE Transactions on Geoscience and Remote Sensing*,
325 41(2), 253-264.
- 326 Aumann, H. H., et al. (2003), AIRS/AMSU/HSB on the Aqua mission: design, science objectives,
327 data products, and processing systems, *IEEE Transactions on Geoscience and Remote Sensing*,
328 41(2), 253-264.
- 329 Biraud, S. C. (2016), ARM-ACME V: ARM Airborne Carbon Measurements V on the North Slope
330 of Alaska Field Campaign ReportRep., 15 pp, DOE Office of Science Atmospheric Radiation
331 Measurement (ARM) Program (United States).
- 332 Boitsov, V. D., A. L. Karsakov, and A. G. Trofimov (2012), Atlantic water temperature and
333 climate in the Barents Sea, 2000–2009, *ICES Journal of Marine Science*, 69(5), 833-840.
- 334 Carmack, E., and F. McLaughlin (2011), Towards recognition of physical and geochemical change
335 in Subarctic and Arctic Seas, *Progress in Oceanography*, 90(1–4), 90-104.
- 336 Chang, R. Y.-W., et al. (2014), Methane emissions from Alaska in 2012 from CARVE airborne
337 observations, *Proceedings of the National Academy of Sciences*, 111(47), 16694-16699.
- 338 Clerbaux, C., et al. (2009), Monitoring of atmospheric composition using the thermal infrared
339 IASI/MetOp sounder, *Atmospheric Chemistry and Physics*, 9, 6041-6054.
- 340 Comiso, J. C., C. L. Parkinson, R. Gersten, and L. Stock (2008), Accelerated decline in the Arctic
341 sea ice cover, *Geophysical Research Letters*, 35(1), L01703.
- 342 Crevoisier, C., et al. (2014), Towards IASI-New Generation (IASI-NG): Impact of improved
343 spectral resolution and radiometric noise on the retrieval of thermodynamic, chemistry and
344 climate variables, *Atmospheric Measurement Techniques*, 7(12), 4367-4385.
- 345 Gambacorta, A. (2013), The NOAA Unique CrIS/ATMS Processing System (NUCAPS):
346 Algorithm Theoretical Basis DocumentationRep., 78 pp, NOAA, NOAA Center for Weather
347 and Climate Prediction.
- 348 Gammelsrød, T., Ø. Leikvin, V. Lien, W. P. Budgell, H. Loeng, and W. Maslowski (2009), Mass
349 and heat transports in the NE Barents Sea: Observations and models, *Journal of Marine*
350 *Systems*, 75(1-2), 56-69.
- 351 Gawarkiewicz, G., and A. J. Plueddemann (1995), Topographic control of thermohaline frontal
352 structure in the Barents Sea Polar Front on the south flank of Spitsbergen Bank, *Journal of*
353 *Geophysical Research: Oceans*, 100(C3), 4509-4524.
- 354 IASI-NG (2017), IASI-NG: Innovative future instrument for studying Earth's atmosphere, edited,
355 Centre National D'Etudes Spatiales.
- 356 Jacob, D. J., A. J. Turner, J. D. Maasackers, J. Sheng, K. Sun, X. Liu, K. Chance, I. Aben, J.
357 McKeever, and C. Frankenberg (2016), Satellite observations of atmospheric methane and
358 their value for quantifying methane emissions, *Atmospheric Chemistry Physics*, 16(22), 14371-
359 14396.

360 Kolstad, E. W. (2008), A QuikSCAT climatology of ocean surface winds in the Nordic seas:
361 Identification of features and comparison with the NCEP/NCAR reanalysis, *Journal of*
362 *Geophysical Research: Atmospheres*, 113(D11), D11106.

363 Kort, E. A., C. Frankenberg, C. E. Miller, and T. Oda (2012), Space-based observations of
364 megacity carbon dioxide, *Geophysical Research Letters*, 39(17), L17806.

365 Leifer, I., and R. Patro (2002), The bubble mechanism for methane transport from the shallow
366 seabed to the surface: A review and sensitivity study, *Continental Shelf Research*, 22(16),
367 2409-2428.

368 Leifer, I., D. Chernykh, N. Shakhova, and I. Semiletov (2017), Sonar gas flux estimation by bubble
369 insonification: Application to methane bubble flux from seep areas in the outer Laptev Sea,
370 *The Cryosphere*, 11(3), 1333-1350.

371 Li, S., and T. A. McClimans (1998), The effects of winds over a barotropic retrograde slope
372 current, *Continental Shelf Research*, 18(5), 457-485.

373 Lien, V. S., F. B. Vikebø, and Ø. Skagseth (2013), One mechanism contributing to co-variability
374 of the Atlantic inflow branches to the Arctic, *Nature Communications*, 4, 1488.

375 Lien, V. S., P. Schlichtholz, Ø. Skagseth, and F. B. Vikebø (2017), Wind-driven Atlantic water
376 flow as a direct mode for reduced Barents Sea ice cover, *Journal of Climate*, 30(2), 803-812.

377 Loeng, H. (1991), Features of the physical oceanographic conditions of the Barents Sea, *Polar*
378 *Research*, 10(1), 5-18.

379 Loeng, H., V. Ozhigin, and B. Ådlandsvik (1997), Water fluxes through the Barents Sea, *ICES*
380 *Journal of Marine Science*, 54(3), 310-317.

381 Maslowski, W., D. Marble, W. Walczowski, U. Schauer, J. L. Clement, and A. J. Semtner (2004),
382 On climatological mass, heat, and salt transports through the Barents Sea and Fram Strait from
383 a pan-Arctic coupled ice-ocean model simulation, *Journal of Geophysical Research: Oceans*,
384 109(C3).

385 Mau, S., et al. (2017), Widespread methane seepage along the continental margin off Svalbard -
386 from Bjørnøya to Kongsfjorden, *Scientific Reports*, 7, 42997.

387 McClimans, T. A., and J. H. Nilsen (1993), Laboratory simulation of the ocean currents in the
388 Barents sea, *Dynamics of Atmospheres and Oceans*, 19(1), 3-25.

389 McClimans, T. A., B. O. Johannesseen, and J. H. Nilsen (1999), Laboratory simulation of fronts
390 between the various water masses in the Kara Sea, paper presented at Oceanic Fronts and
391 Related Phenomena (Konstantin Federov Memorial Symposium), Intergovernmental
392 Oceanographic Commission (IOC) Workshop Report, UNESCO'99, Pushkin, St. Petersburg,
393 Russia.

394 McClimans, T. A., D. R. Johnson, M. Krosshavn, S. E. King, J. Carroll, and Ø. Grenness (2000),
395 Transport processes in the Kara Sea, *Journal of Geophysical Research: Oceans*, 105(C6),
396 14121-14139.

397 Myhre, C. L., et al. (2016), Extensive release of methane from Arctic seabed west of Svalbard
398 during summer 2014 does not influence the atmosphere, *Geophysical Research Letters*, 43(9),
399 2016GL068999.

400 Norwegian Petroleum Directorate (2016), Resource ReportRep., 56 pp, Norwegian Petroleum
401 Directorate,, Stavanger, Norway.

402 Osterkamp, T. E. (2010), Subsea Permafrost, in *Climate and Oceans*, edited by J. H. Steele, S. A.
403 Thorpe and K. K. Turekian, pp. 252-264, Academic Press, London UK.

404 Oziel, L., J. Sirven, and J. C. Gascard (2016), The Barents Sea frontal zones and water masses
405 variability (1980–2011), *Ocean Science*, 12(1), 169-184.

406 Piechura, J., and W. Walczowski (2009), Warming of the West Spitsbergen current and sea ice
407 North of Svalbard, *Oceanologia*, 51(2), 147-164.

408 Polyak, L., S. Korsun, L. A. Febo, V. Stanovoy, T. Khusid, M. Hald, B. E. Paulsen, and D. J.
409 Lubinski (2002), Benthic foraminiferal assemblages from the Souterhn Kara Sea - A river-
410 influenced Arctic marine environment, *The Journal of Foraminiferal Research*, 32(3), 252-
411 273.

412 Razavi, A., C. Clerbaux, C. Wespes, L. Clarisse, D. Hurtmans, S. Payan, C. Camy-Peyret, and P.
413 F. Coheur (2009), Characterization of methane retrievals from the IASI space-borne sounder,
414 *Atmospheric Chemistry and Physics*, 9(20), 7889-7899.

415 Rekacewicz, P. (2005), Oil and gas development and seabirds colonies in the Barents Region, in
416 *Barentswatch Atlas*, edited, UNEP/GRIDA-Arendal.

417 Shakhova, N., et al. (2013), Ebullition and storm-induced methane release from the East Siberian
418 Arctic Shelf, *Nature Geoscience*, 7, 64-70.

419 Skagseth, Ø., T. Furevik, R. Ingvaldsen, H. Loeng, K. A. Mork, K. A. Orvik, and V. Ozhigin
420 (2008), Volume and heat transports to the Arctic Ocean via the Norwegian and Barents Seas,
421 in *Arctic-Subarctic Ocean Fluxes: Defining the Role of the Northern Seas in Climate*, edited
422 by R. R. Dickson, J. Meincke and P. Rhines, pp. 45-64, Springer Netherlands, Dordrecht.

423 Stedmon, C. A., R. M. W. Amon, A. J. Rinehart, and S. Walker (2011), The supply and
424 characteristics of Colored Dissolved Organic Matter (CDOM) in the Arctic Ocean: Pan Arctic
425 trends and differences, *Marine Chemistry*, 124(1), 108-118.

426 Stiansen, J. E., O. Korneev, O. Titov, P. Arneberg, A. Filin, J. R. Hansen, Å. Høines, and S.
427 Marasaev (2009), Joint Norwegian-Russian environmental status 2008. Report on the Barents
428 Sea Ecosystem. Part II – Complete report *Rep. 1502-8828*, 375 pp, Norwegian Marine Data
429 Center (NMDC).

430 Susskind, J., C. Barnet, J. Blaisdell, L. Iredell, F. Keita, L. Kouvaris, G. Molnar, and M. Chahine
431 (2006), Accuracy of geophysical parameters derived from Atmospheric Infrared
432 Sounder/Advanced Microwave Sounding Unit as a function of fractional cloud cover, *Journal*
433 *of Geophysical Research: Atmospheres*, 111(D9), D09S17.

434 Svendsen, H., et al. (2002), The physical environment of Kongsfjorden–Krossfjorden, an Arctic
435 fjord system in Svalbard, *Polar Research*, 21(1), 133-166.

436 Vinje, T., and Å. S. Kvambekk (1991), Barents Sea drift ice characteristics, *Polar Research*, 10(1),
437 59-68.

438 Walsh, J. E., F. Fetterer, J. Scott Stewart, and W. L. Chapman (2016), A database for depicting
439 Arctic sea ice variations back to 1850, *Geographical Review*, 107(1), 89-107.

440 Wanninkhof, R., and W. R. McGillis (1999), A cubic relationship between air-sea CO₂ exchange
441 and wind speed, *Geophysical Research Letters*, 26(13), 1889-1892.

442 Westbrook, G. K., et al. (2009), Escape of methane gas from the seabed along the West Spitsbergen
443 continental margin, *Geophysical Research Letters*, 36.

444 Westbrook, G. K., et al. (2008), Estimation of gas hydrate concentration from multi-component
445 seismic data at sites on the continental margins of NW Svalbard and the Storegga region of
446 Norway, *Marine and Petroleum Geology*, 25(8), 744-758.

447 Whitehead, J. A., and J. Salzig (2001), Rotating channel flow: Control and upstream currents,
448 *Geophysical & Astrophysical Fluid Dynamics*, 95(3-4), 185-226.

449 Wofsy, S. C. (2011), HIAPER Pole-to-Pole Observations (HIPPO): fine-grained, global-scale
450 measurements of climatically important atmospheric gases and aerosols, *Philosophical*

451 *Transactions of the Royal Society A: Mathematical, Physical and Engineering Sciences*,
452 369(1943), 2073-2086.

453 Worden, J., S. Kulawik, C. Frankenberg, V. Payne, K. Bowman, K. Cady-Peirara, K. Wecht, J.-E.
454 Lee, and D. Noone (2012), Profiles of CH₄, HDO, H₂O, and N₂O with improved lower
455 tropospheric vertical resolution from Aura TES radiances, *Atmospheric Measurement*
456 *Techniques*, 5, 397-411.

457 Xiong, X., C. D. Barnet, Q. Zhuang, T. Machida, C. Sweeney, and P. K. Patra (2010), Mid-upper
458 tropospheric methane in the high Northern Hemisphere: Spaceborne observations by AIRS,
459 aircraft measurements, and model simulations, *Journal of Geophysical Research:*
460 *Atmospheres*, 115(D19), D19309.

461 Xiong, X., C. Barnet, E. S. Maddy, A. Gambacorta, T. S. King, and S. C. Wofsy (2013), Mid-
462 upper tropospheric methane retrieval from IASI and its validation, *Atmospheric Measurement*
463 *Techniques*, 6(9), 2255-2265.

464 Yamamoto-Kawai, M., F. A. McLaughlin, E. C. Carmack, S. Nishino, and K. Shimada (2008),
465 Freshwater budget of the Canada Basin, Arctic Ocean, from salinity, δ18O, and nutrients,
466 *Journal of Geophysical Research: Oceans*, 113(C1), C01007.

467 Yurganov, L., I. Leifer, and C. Lund-Myhre (2016), Seasonal and interannual variability of
468 atmospheric methane over Arctic Ocean from satellite data, *Current Problems in Remote*
469 *Sensing of Earth from Space (Sovremennye Problemy Distantionnogo Zondirovaniya Zemli*
470 *iz Kosmosa)*, 13(2), 107-119.

471